



Role of Zinc in Enhancing the Corrosion Resistance of Mg-5Ca Alloys

Nguyen Dang Nam^z

Petroleum Department, PetroVietnam University, Ba Ria City, Ba Ria - Vung Tau Province 74000, Viet Nam

Mg-5Ca-xZn alloys were prepared using various zinc contents from 1 to 5 wt% for use as degradable biomaterials in medical implant applications. The influence of zinc on the corrosion properties of Mg-5Ca alloys prepared in Hanks' solution was examined using electrochemical and surface analysis techniques. The electrochemical tests reveal that the addition of zinc improves the corrosion resistance of Mg-5Ca alloys compared with untreated alloys. The improved corrosion resistance is attributed to the increased refinement of the precipitates, the grain refinement, and the continuous precipitation of Mg-Ca and MgCaZn compounds as a corrosion barrier.

© 2015 The Electrochemical Society. [DOI: [10.1149/2.0281603jes](https://doi.org/10.1149/2.0281603jes)] All rights reserved.

Manuscript submitted May 12, 2015; revised manuscript received December 4, 2015. Published December 12, 2015.

Metallic alloys have become important biomedical materials due to their unique combination of strength, ductility, fatigue resistance and reliability.¹⁻⁴ Magnesium alloys are an ideal material for biomedical applications such as implants and stents⁵⁻⁸ due to their low density (less than 2 g/cm³) and elastic modulus, which are similar to those of human bones.⁹ Importantly, magnesium alloys have high biocompatibility and are biodegradable as well as economical and light. Unfortunately, their low corrosion resistance and formability are serious disadvantages because they form soluble magnesium hydroxide, magnesium chloride and hydrogen gas.¹⁰ In particular, potentially harmful hydrogen gas pockets form and inhibit bone growth during the corrosion process via the $Mg + 2H_2O \rightarrow Mg^{2+} + 2OH^- + H_2$ corrosion reaction.¹⁰ Therefore, improving the corrosion resistance of magnesium and its alloys is an interesting subject of studies with a goal of attaining the required corrosion resistance and a reduced hydrogen-evolution rate, which are key for biomedical applications.⁵

Many investigations have focused on improving the corrosion resistance of magnesium alloys via using surface treatments,¹¹⁻¹² controlling orientation,^{13,14} controlling microstructure,¹⁵⁻¹⁷ and using alloying elements.¹⁸⁻²⁵ Among these methods, the use of alloying elements in a solid solution strongly influences the corrosive and mechanical properties of magnesium alloys.¹⁸⁻²⁵ For these reasons, many magnesium alloys have been developed and investigated. For biomaterial applications, among the different alloying elements of magnesium alloys,²⁶⁻³⁰ calcium appears to be an ideal component because it acts as an active element with reduction potentials close to that of Mg; in addition, it is nontoxic and is an essential element for humans.³¹⁻³⁵ The density of magnesium-calcium (Mg-Ca) alloys is close to that of human bone. Furthermore, Mg-Ca alloys have been recommended as a unique alloying addition to magnesium alloys in the context of medical implants due to its similar Young's modulus to cancellous bones as well as its good biocompatibility and mechanical properties. The microstructure of Mg-Ca systems includes α -Mg and Mg₂Ca phases in which Mg₂Ca is a more active phase than α -Mg, indicating a contradictory electrochemistry with other intermetallic phases such as Mg₁₇Al₁₂, in a Mg-Al system. This phenomenon suggests that the Mg₂Ca phase in Mg-Ca systems acts as an anode, whereas other intermetallic phases, such as Mg₁₇Al₁₂, are assumed to act as the cathode in other Mg alloy systems.³⁵ Unfortunately, in both in vivo and in vitro experiments, the Mg-Ca implants quickly corrode in a saline environment and in human organisms.³⁵ Moreover, binary Mg-Ca alloy with high concentration of Ca indicated high degradation rate and low corrosion resistance. In view of this, Li et al.³⁶ showed that as-cast Mg-5Ca alloy is very brittle at room temperature and the plate samples can be easily broken by bare hands, thus only the Mg-Ca alloys with low Ca contents are suitable for implant application. Thus, the critical subject of interest is the development of new biodegradable implants that can achieve the required corrosion resistance for biomaterial applications. Many techniques, such as the formation of polymers including

poly-L-lactic acid, have been attempted to improve the corrosion resistance of Mg-Ca alloys.³⁷ However, the resulting alloys have limited use due to insufficient mechanical strength.

Recently, it has been reported that the addition of zinc to Mg-Ca alloys remarkably improves their mechanical properties,⁷⁻⁹ enabling them to satisfy the requirements of degradable biomaterials in medical implant applications. Zinc can also form bonds with a greater degree of equivalence, making it an element of exceptional biological and public health importance.³⁸ In addition, some zinc properties are chemically similar to magnesium, such as their similar ion size and common oxidation state of +2. Zinc also forms more stable complexes with N- and S-donors compared with Mg.³⁹ Furthermore, zinc plays ubiquitous biological roles and can interact with many organic ligands.³⁸ Thus, Zn has been strongly considered as an alloying element to improve the corrosion behavior of Mg-Ca alloys. Several studies⁴⁰⁻⁴² revealed that ternary Mg-Zn-Ca alloys in the form of bulk metallic glasses showed good cell viability and no clinically observable hydrogen production in their in vitro and in vivo degradation tests. Furthermore, metallic glasses are brittle, which might lead to reduce the overall biocompatibility.⁴³ However, Mg-Zn-Ca bulk metallic glasses with high content of Zn could be harmful to the human body due to biodegradation.⁴⁴ Recently, crystalline Mg-Zn-Ca alloys have been considered as biomaterials in biodegradable implant.^{45,46} They reported that the ternary intermetallic compounds can improve the corrosion resistance in a simulated body blood environment. These studies exposed the limited phenomenological analyses. However, the optimal compositions of Mg-Zn-Ca alloys for clinical applications have not been reached yet. In this study, we developed Mg-5Ca-xZn biomaterials with good medically acceptable corrosion rate in Hanks' solution, which was assessed by the electrochemical properties and microstructure of constituent phases using electrochemical and surface characterization methods. A detailed investigation of the corrosion behavior and the mechanism in Hanks' solution was performed.

Experimental

Specimen preparation.— All of the test specimens of Mg-5Ca-xZn were prepared under a mixture of CO₂ and SF₆, and Zn was added in varying amounts (x = 1, 3, 4 and 5 wt%). The molten metal was cast and stirred after being maintained at 800°C for 60 min and was then allowed to cool for 20 min. The chemical compositions of tested alloys were determined by optical emission spectroscopy. Alloys with chemical compositions were 5.105 Ca, 0.005 Si, 0.002 Fe, 0.003 Cu, 0.007 Ni, 0.061 Mn and Mg balance, while the difference between measured and specified composition of Zn is imperceptible. It is noted that the Fe/Mn ratio, which seems to be a critical factor, is an important parameter for the corrosion of magnesium alloys. This factor will not affect the corrosion properties of magnesium alloys if it reaches around 0.032.^{47,48} In this study, the Fe/Mn ratio is closed to that value, indicating that at these concentrations of iron and manganese, the corrosion of magnesium alloys should not be governed by iron and

^zE-mail: namnd@pvu.edu.vn

Table I. Chemical composition of Hanks' solution.

Compound	g/l
NaCl (Sodium chloride)	8.00
KCl (Potassium chloride)	0.40
NaHCO ₃ (Sodium hydrogen carbonate)	0.35
NaH ₂ PO ₄ · H ₂ O	0.25
Na ₂ HPO ₄ · 2H ₂ O	0.06
MgCl ₂ (Magnesium chloride)	0.19
MgSO ₄ · 7H ₂ O (Magnesium sulfate heptahydrate)	0.06
Glucose	1.00
CaCl ₂ · 2H ₂ O (Calcium chloride dihydrate)	0.19

manganese contents. The specimens used for corrosion tests were finished by grinding with 1200-grit silicon carbide paper. For the observation of the microstructure, the specimens were finished by grinding with 4000-grit silicon carbide paper and then polishing with 0.5 µm alumina powders. These specimens were then etched in 0.008 mol/dm³ HNO₃ for 10 s.

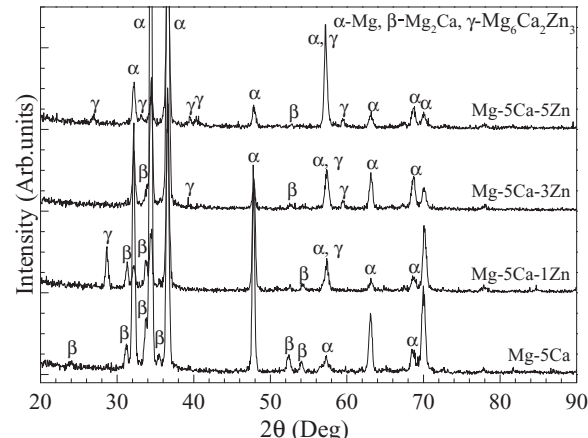
Electrochemical investigation methods.— All of the experiments were performed in 1000 ml Hanks' solution (pH 7.4, see Table I for the composition) at 37°C. The exposed area was 1 cm². Potentiodynamic polarization and potentiostatic tests were performed using a VSP system (BioLogic Scientific Instruments). The electrochemical test cell consists of a specimen, a saturated calomel electrode (SCE) and two graphite rods as the working, reference and counter electrodes, respectively. Prior to the potentiodynamic polarization test, the samples were exposed to the solution for 1 h to stabilize the open-circuit potential. The potential of the electrodes was swept at a rate 0.166 mV/s in the range from the initial potential of -250 mV versus E_{OCP} to the final potential. Electrochemical impedance spectroscopy (EIS) was performed at the steady open circuit potential with a peak-to-peak amplitude of the sinusoidal perturbation of 10 mV and a frequency range from 100 kHz to 10 mHz using the VSP system with a commercial software program for the AC measurements. Tests were conducted every hour over a period of 10 h.

Hydrogen evolution tests.— The hydrogen evolution rate of the Mg-5Ca-xZn alloys was investigated by immersion tests. The specimens, with dimensions of 10 mm × 10 mm × 3 mm, were prepared by grinding each side with 1200-grit silicon carbide (SiC) paper and degreasing the surfaces with ethanol prior to corrosion testing in Hanks' solution with a pH of 7.4 at 37°C. The amount of hydrogen evolution was used as an indicator of the corrosion rate which was monitored after 1 hour. To ensure reproducibility, three measurements were run for electrochemical and immersion tests.

Surface analyses.— The crystal structure of the as-received specimens was investigated by XRD (XRD Model D/MAX-RC) using Cu K_α radiation. The corresponding microstructures were observed by electron probe microanalysis (EPMA) after being polished with 0.5 µm alumina powder. The corresponding microstructures were observed by scanning electron microscopy/energy dispersive spectroscopy (SEM/EDS Supra 55 VP) after etching. To investigate the relationship between the electrochemical behavior and the surface morphology, the specimens were examined using SEM/EDS after pitting was initiated. The specimen surfaces were also examined by X-ray photoelectron spectroscopy (AES-XPS ESCA2000) after 1 h of exposure to the open-circuit potential.

Results and Discussion

Alloy microstructure and composition.— The crystal structural composition of the Mg-5Ca-xZn specimens was examined using XRD, and the results are shown in Fig. 1. There is a significant difference in the α-Mg peaks between the Mg-5Ca and Zn-containing specimens. The intensity of α-Mg peaks decreases with increasing Zn

**Figure 1.** XRD patterns of Mg-5Ca-xZn alloys.

content. The Zn specimens include Zn-containing phases formed via the interaction of Zn with Mg and Ca to form a MgCaZn compound⁴⁹ verified using PANDAT software. This would result in a change in the Mg₂Ca phase in the specimens containing Zn because the added Zn interacted with Mg and to form the Mg₆Ca₂Zn₃ intermetallic compound at the grain boundaries. The Mg₆Ca₂Zn₃ phase was observed in all of the Zn-containing specimens, and the intensities of the Mg₆Ca₂Zn₃ diffraction peaks increased as the Zn content increased. In the solidification process, Ca and Zn should be completely melted in the magnesium, resulting in the substantial development of precipitation. The precipitation distributions can be observed in the SEM/EDS and EPMA results.

The microscopic examinations of Mg-5Ca-xZn were performed using EPMA mapping after micro polishing. EPMA analysis showed the elemental distribution of Mg, Ca, and Zn in the alloy microstructure, as shown in Fig. 2. Ca and Zn were enriched in the grain boundary regions, indicating the Mg₂Ca and Mg₆Ca₂Zn₃ precipitation formation. The microstructures of the Mg-5Ca alloys with different amounts of Zn are compared in Fig. 3. The results indicate that a markedly sharper edge of the grain and precipitation refinement are observed in the Mg-5Ca-1Zn specimen, while the preferred circular shapes of the grain and larger precipitations are observed in the Mg-5Ca, Mg-5Ca-3Zn and Mg-5Ca-5Zn specimens. Furthermore, wide dendrite precipitation was also observed in Mg-5Ca specimens. The precipitation distributions are also confirmed by SEM/EDS, as shown in Fig. 4 and Table II, revealing the presence of a Ca-rich precipitation located at the grain boundary in the Mg-5Ca specimen in Fig. 4a, whereas Ca-rich and Zn-rich precipitations are observed in the Mg-5Ca-5Zn specimen, as shown in Fig. 4b. The EDS analysis is also given in Table II. Microstructure and composition analyses indicate that the refinement of the dispersed precipitates was observed in the Mg-5Ca-1Zn specimen, whereas this refinement was not observed in the case of higher Zn-containing specimens. The presence of Zn dispersoids in the microstructure is highly effective in promoting the formation of a kinetic barrier layer to improve the corrosion resistance.

Overall, the alloy microstructures included primary α grains surrounded by a eutectic mixture of α and dispersed precipitates. The specimens had relative grain refinement, refinement of the dispersed precipitate, and continuous precipitation with decreasing Zn content. These factors could influence the overall electrochemical corrosion performance because the dispersed precipitate is expected to function as a kinetic barrier.

Corrosion resistance.— Figure 5a presents the polarization curves of the Mg-5Ca alloys as a function of the Zn content in Hanks' solution. All of the specimens exhibited active behavior as indicated by an increase in the anodic current with increasing potential, suggesting the absence of a passive film on the alloy surfaces in the investigated

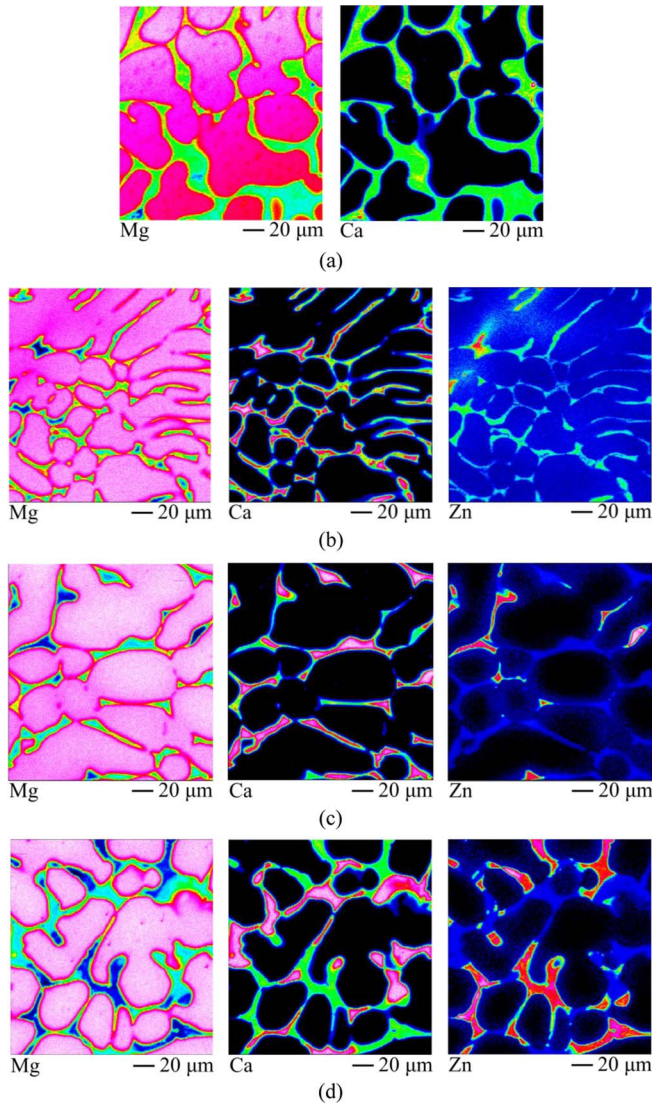


Figure 2. EPMA mapping of alloying elements on the surface of the specimens: (a) Mg-5Ca, (b) Mg-5Ca-1Zn, (c) Mg-5Ca-3Zn, and (d) Mg-5Ca-5Zn alloys.

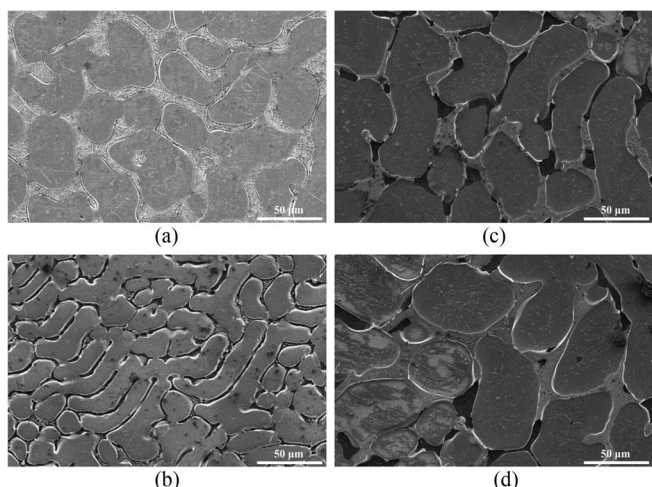


Figure 3. SEM micrographs of (a) Mg-5Ca, (b) Mg-5Ca-1Zn, (c) Mg-5Ca-3Zn, and (d) Mg-5Ca-5Zn alloys.

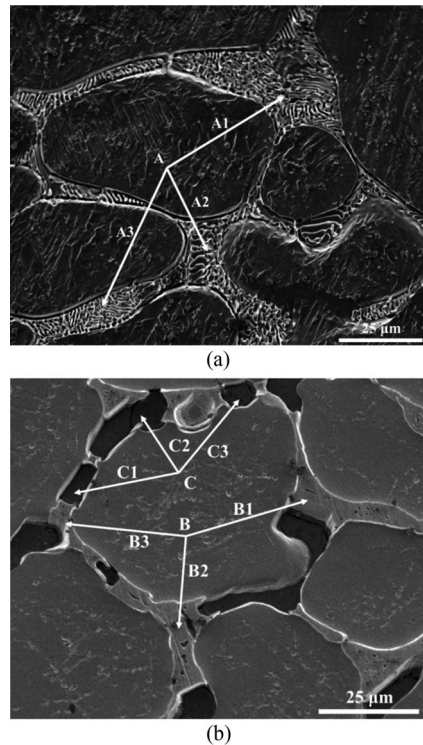


Figure 4. SEM/EDS measurements of the precipitates in (a) Mg-5Ca-based and (b) Mg-5Ca-5Zn alloys.

solution. The results indicate that the addition of Zn from 0 to 5 wt% increased the corrosion potential and decreased the corrosion current density as the Zn addition decreased. Table III lists the corrosion properties, and Figure 5b shows the change in corrosion rates of the Mg-5Ca-xZn alloys. The results suggest that the addition of Zn improves the corrosion resistance of the Mg-5Ca-based alloy. The polarization resistance (R_p) and average corrosion rate were determined using the Tafel extrapolation method, based on Faraday's law, as follows:^{50,51}

$$R_p = \frac{\beta_a \times \beta_c}{2.3 \times i_{corr} \times (\beta_a + \beta_c)}$$

$$\text{Corrosion rate (mm/yr)} = \frac{3.27 \times 10^{-3} \times i_{corr} \times E.W}{D}$$

where i_{corr} is the corrosion current density ($\mu\text{A}/\text{cm}^2$), E.W. is the equivalent weight in grams, and D is the density of the metal (g/cm^3). The Zn-containing specimens showed lower corrosion rates than the Mg-5Ca-based alloy, and the corrosion rate decreased with a decrease in Zn content. The average corrosion rate of the specimens was ranked

Table II. EDS analysis of the intermetallic particles in Fig. 4.

Peaks	Element (wt%)			
	Mg	Ca	O	Zn
A1	58.3	29.4	10.3	-
A2	56.8	24.6	12.6	-
A3	59.9	28.6	11.5	-
B1	55.7	30.5	6.6	7.2
B2	55.0	28.5	7.2	9.3
B3	55.1	28.7	6.3	9.9
C1	28.7	5.3	49.6	16.4
C2	29.7	6.0	50.2	14.1
C3	25.1	5.0	48.2	21.7

Table III. Corrosion properties of Mg-5Ca-xZn alloys in Hanks' solution (pH 7.3) at 37°C obtained from the polarization curve.

Specimen		E_{corr} (mV _{SCE})	i_{corr} ($\times 10^{-6}$ A/cm ²)	β_a (mV/decade)	$-\beta_c$ (mV/decade)	R_p ($\Omega \cdot \text{cm}^2$)
Mg-5Ca	1 st	-1570	59.4	176	298	801
	2 nd	-1560	69.4	183	287	700
	Average	-1575	64.4			750
Mg-5Ca-1Zn	1 st	-1500	9.1	55	217	2096
	2 nd	-1520	10.6	56	222	1834
	Average	-1510	9.9			1965
Mg-5Ca-3Zn	1 st	-1470	13.2	59	258	1582
	2 nd	-1490	14.1	58	269	1471
	Average	-1480	13.6			1526
Mg-5Ca-5Zn	1 st	-1450	16.8	61	277	1294
	2 nd	-1440	18.6	59	275	1136
	Average	-1445	17.7			1215

in the following order: base alloy > Mg-5Ca-5Zn > Mg-5Ca-3Zn > Mg-5Ca-1Zn. This improvement could be related to the formation of a protective layer on the alloy surface.

Figure 6 shows the Nyquist plots obtained from alloy electrodes after a 10-h immersion in Hanks' solution at 37°C. Higher impedance values were observed for the Zn-containing alloy electrodes (Figs. 6b, 6c and 6d) compared with that of the Mg-5Ca-based alloy (Fig. 6a), and these values are consistent with the potentiodynamic polarization

results. The high-frequency spectra detect the local surface defects, whereas the medium- and low-frequency spectra detect the process within the protective layer and the process of the metal/protective layer interface, respectively.⁵²⁻⁵⁴ The increase in the arc diameter suggests that there is an improvement in the protective layer. The results show that the addition of Zn improved the formation of the protective layer.

Additional information can be obtained about the electrochemical processes occurring at the solution-electrode interface with a detailed analysis of the EIS using suitably designed equivalent circuits. Figure 7 shows the equivalent circuit that was used to fit the EIS data, where R_s represents the solution resistance, CPE represents the constant phase element, R_f is the protective layer resistance, and R_{ct} is the charge transfer resistance, as shown in equivalent circuit 1 in Fig. 8. The high- (R_f) and low- (R_{ct}) frequency resistance components were affected by the Zn alloying element. In addition, L denotes the inductance, and R_L represents the corresponding resistance, as shown in equivalent circuit 2 in Fig. 7. These parameters were added when the negative impedance was observed at low frequencies. In this case, the capacitor was replaced with a CPE to improve the fitting quality in which the CPE contained a double-layer capacitance (C) and the phenomenological coefficient (n). The n value of a CPE indicates its meaning, as follows: n = 1, a capacitance; n = 0.5, a Warburg impedance; n = 0, a resistance and n = -1, an inductance. In the present study, n was consistently maintained near 0.8 of the deviation from ideal dielectric behavior. Furthermore, n appears to be associated with the non-uniform distribution of current resulting from roughness and surface defects and reflects the degree of "non-ideality" of the double layer capacitance or the extent of the depression of the semi-circles in the Nyquist plots.^{53,54} The Zsimpwin program was used to fit the EIS data to determine the optimized values for the protective layer and charge transfer resistance parameters (R_f and R_{ct}), which are presented in Fig. 8. The variation of the protective layer resistance (R_f) with the immersion time for Mg-5Ca-xZn is provided in Fig. 8a. It can be observed that the protective layer resistance increases steadily as the immersion time increases during the initial 6 h and then decreases for the Mg-5Ca-based alloy, while the protective layer resistances increase steadily as the immersion time increases and as the Zn addition decreases. This result indicates that the decreasing Zn content increases not only the protective layer resistance but also its stability. Fig. 8b shows the charge transfer resistances, which also increase as the immersion time increases and as the Zn addition decreases, indicating good corrosion resistance.

Figures 9a and 9b show the hydrogen evolution measurements and corrosion rate curves of the Mg-5Ca-xZn specimens immersed in Hanks' solution (pH 7.4) at 37°C. The hydrogen evolution rate, V_H (ml/cm².d) could be related to the corrosion rate as, P_H (mm/yr) = 2.279 V_H .⁵⁵ As shown in Figure 9, the hydrogen-evolution test and corrosion rate revealed that the addition of Zn generated a significant

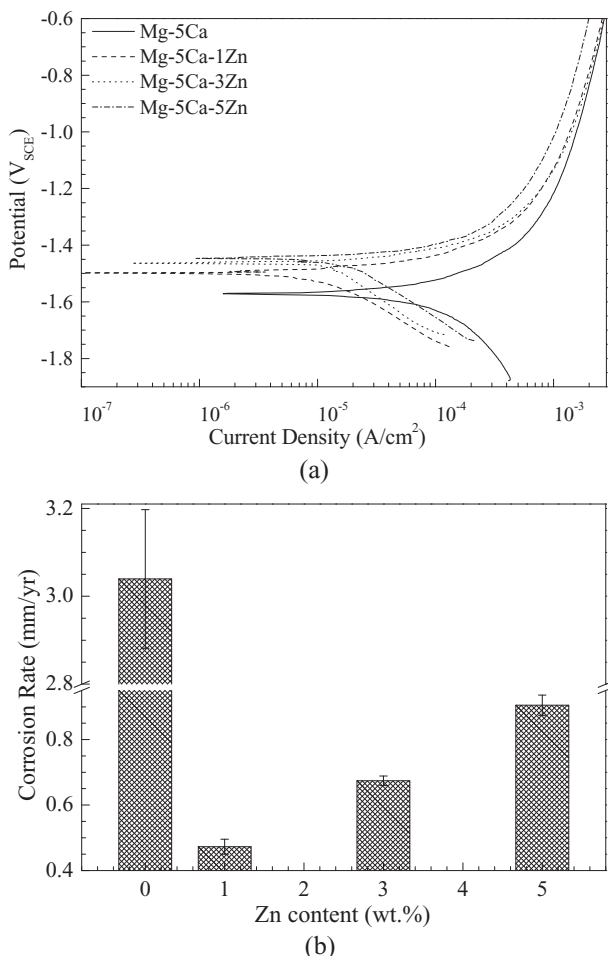


Figure 5. (a) Potentiodynamic polarization and (b) effect of Zn on the corrosion rate of Mg-5Ca alloy in Hanks' solution at 37°C.

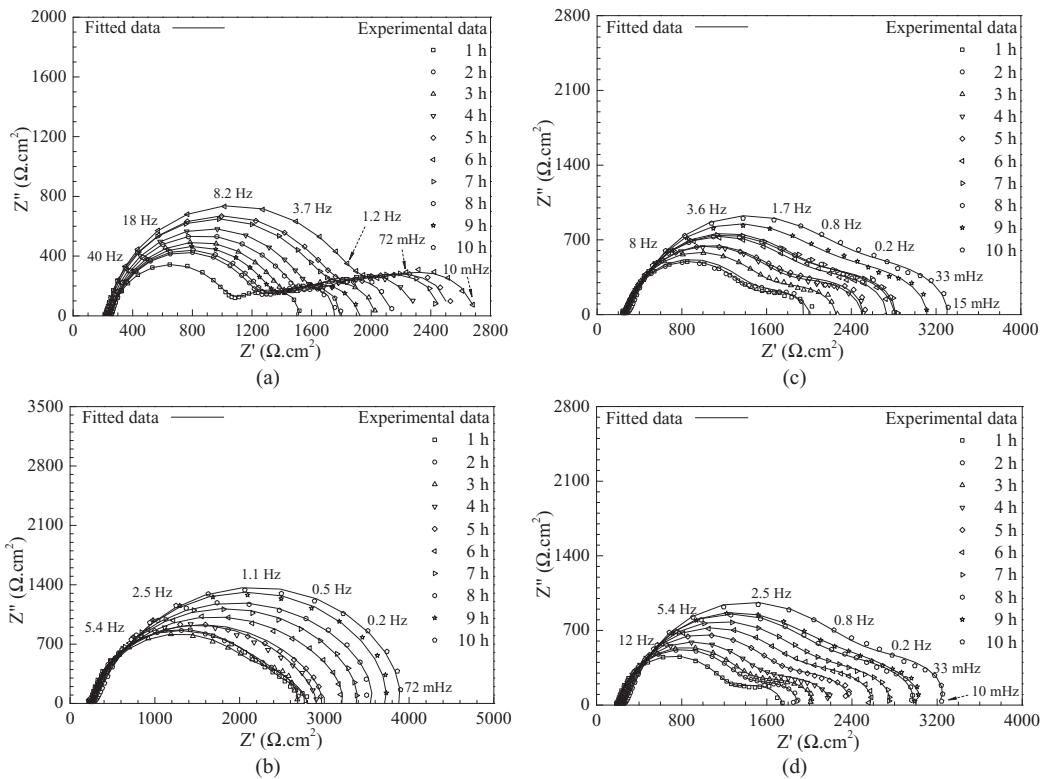


Figure 6. Nyquist plots of (a) Mg-5Ca, (b) Mg-5Ca-1Zn, (c) Mg-5Ca-3Zn, and (d) Mg-5Ca-5Zn alloys.

change in behavior of Mg-5Ca-based alloy. The results showed that Mg-5Ca-based alloy featured strong gas evolution during degradation in Hanks' solution (pH 7.4) at 37°C, whereas Zn-containing alloys induced a remarkable reduction in the amount of hydrogen evolved, with the best corrosion resistance being observed at 1 wt%. Therefore, the results obtained from hydrogen-evolution test indicate that an increased Zn content decreased the corrosion resistance, supporting the results of the electrochemical tests (Figs. 5, 6 and 8).

Figure 10 shows the SEM images of the surface morphology after a 10-h immersion. There was a significant difference in the surface morphology of the alloy surfaces due to the formation of small pits on the surface, resulting in the inward penetration of ions, such as SO_4^{2-} and Cl^- . Pits were observed on both the Mg-5Ca-based and Mg-5Ca-5Zn alloy surfaces. This degradation is due to a thickening of the protective layer and the subsequent electrochemical corrosion reactions. However, no localized corrosion was observed on the Mg-5Ca-1Zn and Mg-5Ca-3Zn alloy surfaces. To study the pit initiation, the

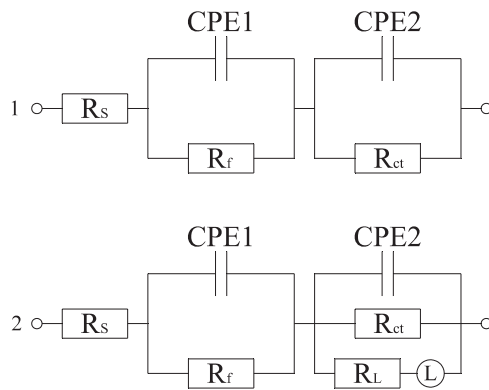


Figure 7. Equivalent circuit model to fit the EIS data.

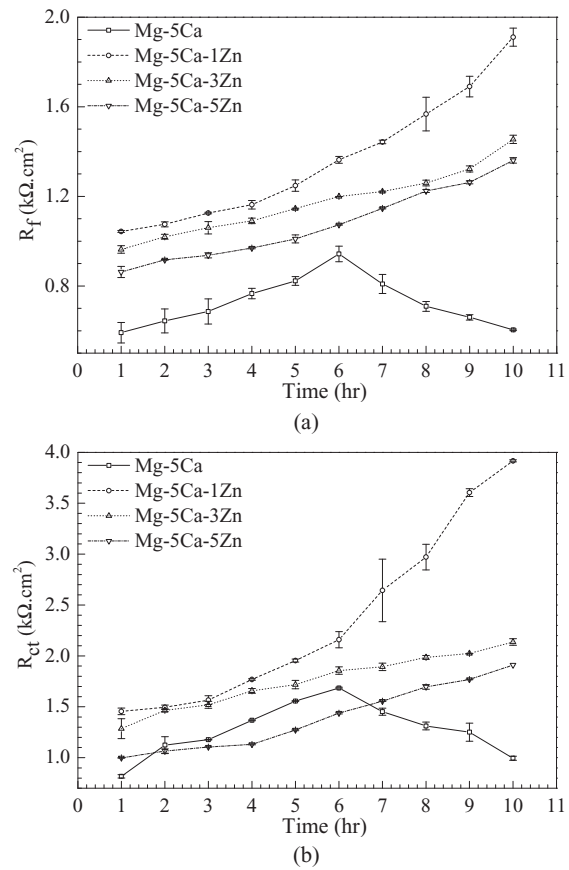


Figure 8. Effects of Zn content on (a) protective layer resistance and (b) charge transfer resistance.

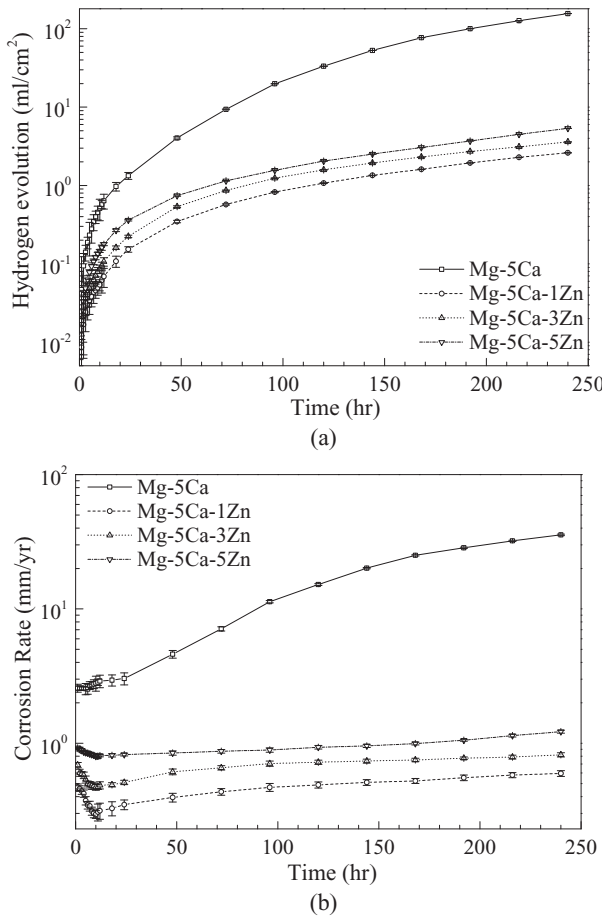


Figure 9. (a) hydrogen evolution measurements and (b) corrosion rate curves of the Mg-5Ca-xZn samples immersed in Hanks' solution at 37°C.

Mg-5Ca-based and Mg-5Ca-5Zn specimens were finished with 4000-grit silicon carbide (SiC) abrasive papers; then, a voltage of $-1300\text{ mV}_{\text{SCE}}$ was applied until bubbles formed on the surface. Then the surface was investigated using SEM/EDS. Figure 11 and Table IV show an SEM/EDS image of the pit initiation, indicating that the galvanic attack of the base alloy surface adjacent to the Mg₂Ca precipitate was observed. It also shows that the particle acts as an anode with respect

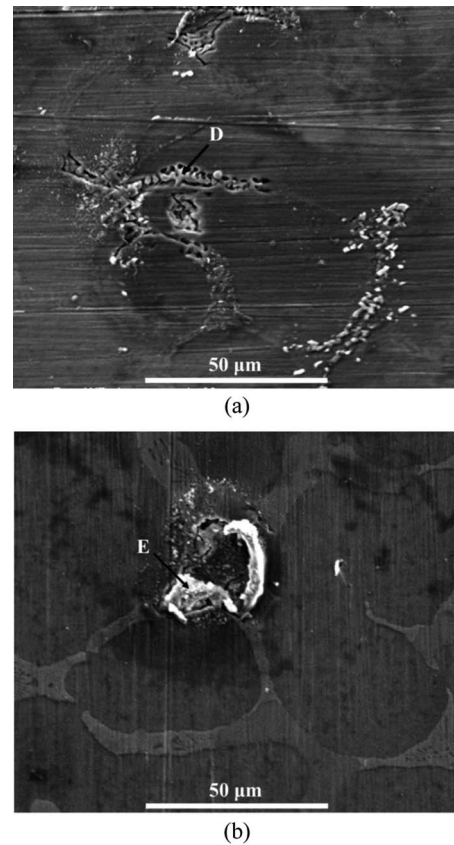


Figure 11. EDS/SEM images of surface morphology after pit initiation: (a) for Mg-5Ca and (b) for Mg-5Ca-5Zn alloys.

to the matrix, which forms a galvanic cell. The SEM/EDS analysis obtained from the Mg-5Ca-based alloy surface is shown in Fig. 11a and Table IV and reveals that some precipitates at the grain boundary were removed from the microstructure. The same results were also observed in the Mg-5Ca-5Zn alloy specimen, as shown in Fig. 11b and Table IV. From the results of the SEM/EDS analyses, the Mg₂Ca and Mg₆Ca₂Zn₃ precipitates play a significant role in pit initiation or pit propagation in Mg-5Ca-xZn alloys. This is the best evidence that the pitting corrosion was initiated around the Mg₂Ca precipitate due to the micro-galvanic corrosion between the precipitates and the α -Mg matrix.

The surface films have been analyzed by XPS measurement after 1 h of exposure to the OCP in Hanks' solution as shown in Fig. 12. The results show that Mg, Ca, Zn, and O peaks exist on the alloy surfaces. Oxygen KLL and KVV correspond to peaks in the region of approximately 1100 and 745 eV^{56,57} as shown in Fig. 12a. The narrow XPS spectra for the Mg 2p, Ca 2p, Zn 2p, and O 1s regions are shown in Figs. 12b–12e, respectively. The results show the chemical compounds detected on the alloy surfaces including MgO, Mg(OH)₂, CaO, Ca(OH)₂, ZnO and Zn(OH)₃,^{58–60} and that these compounds are enriched in the surface of Mg-5Ca-1Zn specimen. The oxide/hydroxide products on the alloy surface are considered to be related to the improvement in the protective films. This result indicates that the

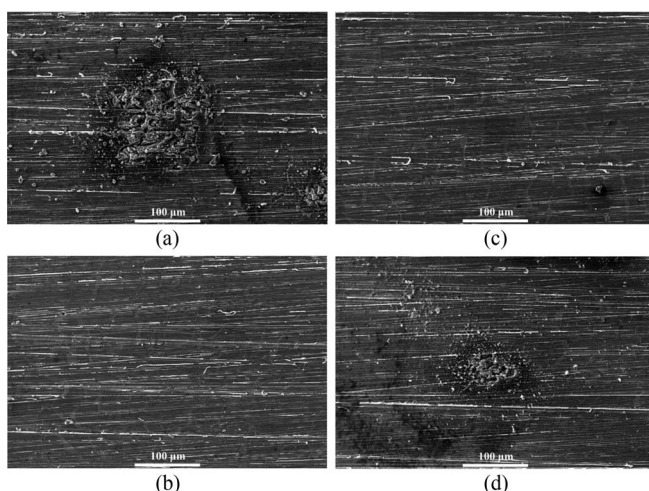


Figure 10. SEM images of (a) Mg-5Ca, (b) Mg-5Ca-1Zn, (c) Mg-5Ca-3Zn, and (d) Mg-5Ca-5Zn alloys.

Table IV. EDS analysis of the intermetallic particles in Fig. 11.

Peaks	Element (wt%)			
	Mg	Ca	O	Zn
D	77.6	13.1	9.3	-
E	27.1	3.9	30.8	38.2

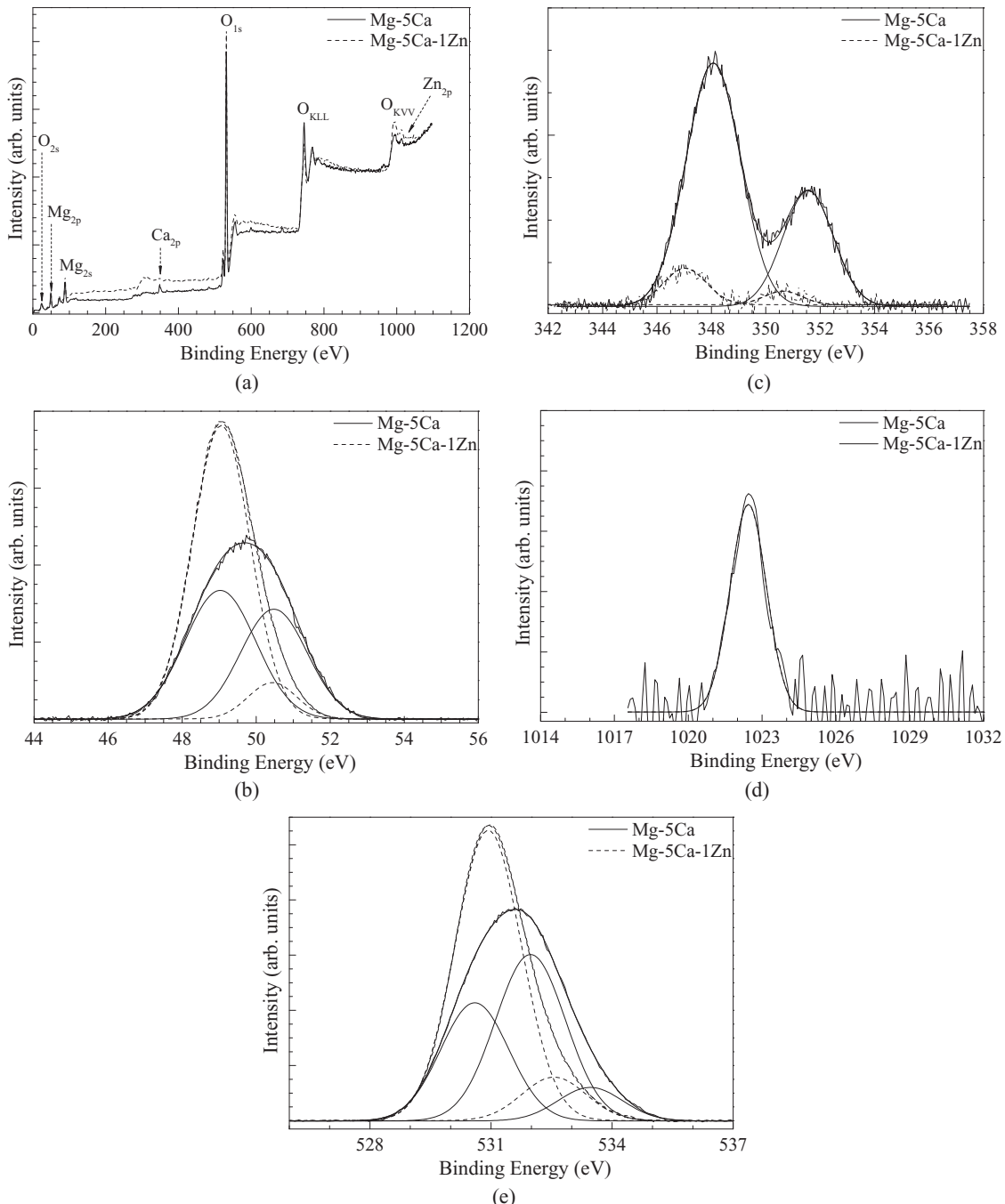


Figure 12. XPS peak analysis for the surface products of the Mg-5Ca-based and Mg-5Ca-1Zn alloys: (a) survey scan spectra and narrow scan spectra of (b) Mg, (c) Ca, (d) Zn, and (e) O.

pitting resistance has been improved by the interactions among the (Mg, Ca, and Zn) oxide/hydroxide products. The enriched oxide/hydroxide products could play the most significant role in improving the protective films of the Mg-5Ca-1Zn specimen with more adhesive and stable passive films.

Discussion.— Ma et al.^{61,62} reported that the solubility of metallic glasses containing alloying elements such as Mg, Zn and Ca is extended, resulting in chemically homogeneous alloys, which can be attained at equilibrium if the molten alloy process includes slow cooling. In this study, the changes that occurred in the microstructure are mainly due to the addition of zinc, which refines the precipitates and grain size. Three microstructural constituents were found,

including α -Mg, Mg₂Ca and Mg₆Ca₂Zn₃ precipitates, in the alloy microstructures. These micro constituents are clearly shown in the microstructure results given in Figs. 1–4. In addition, the Mg₂Ca precipitate was reported to exhibit a more anodic potential than that of the α -Mg matrix.³⁵ Thus, in Zn-containing alloys, the size and spatial distribution of the precipitates, along with the continuous combination of Mg₂Ca and Mg₆Ca₂Zn₃ precipitates, cause the surface to be more electrochemically heterogeneous in the Mg-5Ca alloy as the Zn addition decreases. In addition, microporosity has been observed when zinc addition increases. It can be attributed to the melt zinc atoms in the solidification process which were rejected by the growing α -Mg and enriched in the residual liquid. It also affects the corrosion resistance of Mg-5Ca-xZn alloys. The microstructure results indicate

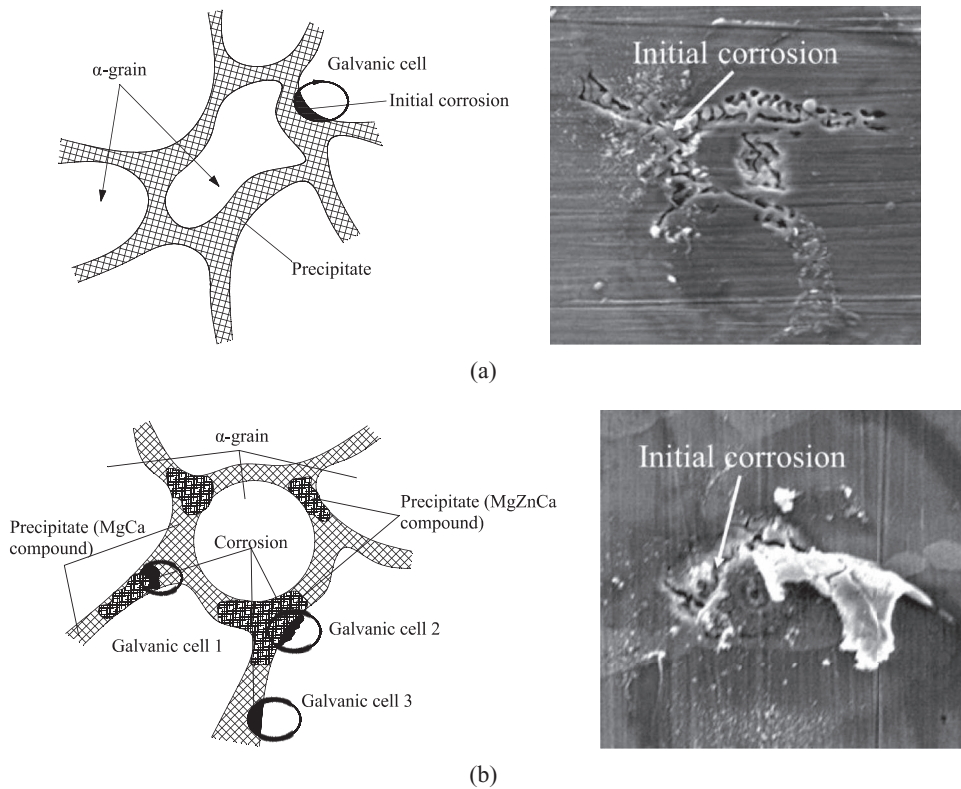


Figure 13. Schematic diagram of local microgalvanic cells created by (a) precipitate-containing anodic impurities in Mg-Ca alloy and (b) precipitate-containing anodic-cathodic impurities in higher zinc-containing specimens.

cate the presence of the $Mg_6Ca_2Zn_3$ phase separate from the Mg_2Ca precipitate at the grain boundaries for the Mg-5Ca-xZn alloys containing 3 wt% Zn and above but do not account for its presence in the 1 wt% Zn alloy. The evidence regarding these precipitates is clear in the SEM/EDS and EPMA results. Thus, the electrochemical behavior of these alloys depends on the microstructure and on how the alloy distributions interact when in contact with a corrosive environment. These changes in alloy microstructures significantly affect the different electrochemical behaviors of the Mg alloys prepared with different amounts of Zn content.

Hanks' solution is an aggressive environment for the magnesium alloys due to the chloride ion participation in the dissolution reaction. Chloride ions react aggressively with magnesium, calcium and zinc. The chloride ions (critical concentration of approximately 0.002 to 0.02 M) attack the alloy surface and transform oxides/hydroxides into readily soluble salts containing chloride. Among the microconstituents in the Mg-5Ca-xZn alloys, $Mg_6Ca_2Zn_3$ could provide the maximum resistance to a corrosive environment because it functions as a cathode in the electrochemical corrosion process, suggesting that corrosion occurs around this precipitate in both the α -Mg matrix and the Mg_2Ca precipitate. Therefore, this phase influences the overall electrochemical corrosion behavior with different amounts of Zn due to the significant difference in morphology. The high corrosion resistance of Mg-5Ca-1Zn was attained due to the refinement, spatial distribution and continuity of the precipitates. In this case, the $Mg_6Ca_2Zn_3$ precipitate plays a dual role in the electrochemical corrosion behavior of the Mg-5Ca alloy, including providing a microgalvanic corrosion and/or a physical corrosion barrier. For low zinc content, the smaller grain size could reduce the corrosion rate because it facilitates the protective layer formation. In addition, the presence of Zn could form a dense and continuous amorphous layer rich in Zn and oxygen so that the dissolution of the alloy is mitigated. This process indicates that the surface could be protected, resulting a reduced hydrogen production to acceptable levels. In the present study, the grain boundaries can

function as a physical corrosion barrier and can inhibit dissolution of the wall between the grains of the Mg-5Ca-1Zn alloy in Hanks' solution. The microstructure results showed that the Zn addition to the Mg-5Ca alloy alters the distribution of the intermetallic phases, resulting in a close interparticle distance and a net-like feature of the precipitates at the grain boundaries. In contrast, the Mg-5Ca alloy is unable to assume these roles. For higher Zn-containing alloys, the $Mg_6Ca_2Zn_3$ is separated from the Mg_2Ca precipitate but maintains a close interparticle distance and a net-like feature at the grain boundaries, indicating that it is highly cathodic to the Mg_2Ca precipitate, and hydrogen evolution preferentially occurs on the $Mg_6Ca_2Zn_3$ -rich precipitate as the highest effective cathode. This indicates that the pitting corrosion could be initiated and concentrated in the region of the $Mg_6Ca_2Zn_3$ -rich precipitate due to the possible microgalvanic corrosion (i) between the $Mg_6Ca_2Zn_3$ (cathode) and Mg_2Ca precipitates (anode), (ii) between the $Mg_6Ca_2Zn_3$ precipitate (cathode) and α -Mg matrix (anode), and (iii) between the Mg_2Ca precipitate (anode) and the α -Mg matrix (cathode), as shown in Fig. 13a. The possible complex microgalvanic corrosion is described in Fig. 13b. The Mg_2Ca precipitate itself possesses the most anodic potential, while the $Mg_6Ca_2Zn_3$ precipitate must be considered as the most cathodic potential that allows the electrons pass to a certain degree, presenting the possibility for galvanic corrosion. In addition, this process can be faster due to the support of the coupling between the Mg_2Ca precipitate (anode) and the α -Mg matrix. After the Mg_2Ca precipitate is dissolved by the corrosion process, the second galvanic cell is established between the cathodic $Mg_6Ca_2Zn_3$ precipitates and the anodic α -Mg matrix. In the case of higher Zn content, the precipitates are the major cause of pitting corrosion. Considering these results, the improved pitting corrosion resistance as the Zn content decreases could be related to the close interparticle distance, the refinement and net-like feature of the precipitates at the grain boundaries as well as the grain refinement. These factors could result in a physical corrosion barrier that reduces the susceptibility of pitting corrosion.

Conclusions

The significant changes in the alloy microstructure caused by the Zn addition reduce the α -Mg grain size. The precipitation of the discontinuous Mg₂Ca phase at the grain boundaries was inhibited by the high density of a mixture of Mg-Ca and Mg-Ca-Zn compounds in the Zn-containing alloy specimens. A higher density and more continuous precipitation surrounding the finer α -Mg grain size significantly affect the corrosion resistance by controlling the alloy microstructure. In addition to the results of the potentiodynamic test, the corrosion rate of Zn-containing specimens was lower than that of the Mg-5Ca-based alloy, and the rate increased as the Zn content decreased. This result indicates that the addition of Zn improves the corrosion resistance in Hanks' solution (pH 7.3) at 37°C. Furthermore, the EIS measurements indicated that the semicircle was less depressed in the case of the Zn-containing alloy specimens compared with the Mg-5Ca-based alloy. The protective properties and the charge transfer resistance increased as the Zn content decreased. In addition, the biodegradable Mg-5Ca-xZn alloys can control hydrogen evolution remarkably during degradation in Hanks' solution. SEM/EDS analysis clearly shows that the Ca- and Zn-containing phases are the main cause for pit initiation and propagation. In summary, the refinement of grain size and precipitation as well as a high density and more uniform precipitation over the α -Mg matrix were achieved when Zn was added up to 1 wt%, and this addition plays a significant role in improving the surface protective layer of the Mg-5Ca alloy by stabilizing it. However, an increased Zn content decreased the corrosion resistance due to the microstructural changes that hinder the formation of the protective layer.

Acknowledgments

This work is funded by PetroVietnam University under grant code GV1505. The author is grateful to Assoc. Prof. V.T.H Thu from University of Science, P.T.N. Ha from Ton Duc Thang University and M. Vaka from the Deakin University for their thorough editorial work and helpful discussions.

References

- P. Erne, M. Schier, and T. J. Resink, *Cardiovasc. Inter. Rad.* **29**, 11 (2006).
- G. L. Song and A. Atrens, *Adv. Eng. Mater.* **5**, 837 (2003).
- J. R. Scully, A. Gebert, and J. H. Payer, *J. Mater. Res.* **22**, 302 (2007).
- M. P. Staiger, A. M. Pietak, J. Huadmai, and G. Dias, *Biomaterials* **27**, 1728 (2006).
- F. Witte, V. Kaese, H. Haferkamp, E. Switzer, A. Meyer-Lindenberg, C. J. Wirth, and H. Windhagen, *Biomaterials* **26**, 3557 (2005).
- R. Erbel, C. D. Mario, J. Bartunek, J. Bonnier, B. D. Bruyne, F. R. Eberli, P. Erne, M. Haude, B. Heublein, M. Horrigan, C. Ilsley, D. Böse, J. Koolen, T. F. Lüscher, N. Weissman, and R. Waksman, *Lancet* **369**, 1869 (2007).
- M. P. Staiger, A. M. Pietak, J. Huadmai, and George Dias, *Biomaterials* **27**, 1728 (2006).
- R. Zeng, W. Dietzel, F. Witte, N. Hort, and C. Blawert, *Adv. Eng. Mater.* **10**, B3 (2008).
- F. Witte, V. Kaese, H. Haferkamp, E. Switzer, A. Meyer-Lindenberg, C. J. Wirth, and H. Windhagen, *Biomaterials* **26**, 3557 (2005).
- W. C. Kim, J. G. Kim, J. Y. Lee, and H. K. Seok, *Mater. Lett.* **62**, 4146 (2008).
- C. Fei Li, M. J. Wang, W. H. Ho, H. N. Li, and S. K. Yen, *J. Electrochem. Soc.* **158**, C11 (2011).
- J. L. Wang, C. Ke, K. Pohl, N. Birbilis, and X. B. Chen, *J. Electrochem. Soc.* **162**, C403 (2015).
- C. R. McCall, M. A. Hill, and R. S. Lillard, *Corros. Eng. Sci. Technol.* **40**, 337 (2005).
- K. S. Shin, M. Z. Bian, and N. D. Nam, *JOM* **64**, 664 (2012).
- A. D. Südholz, N. T. Kirkland, R. G. Buchheit, and N. Birbilis, *Electrochem. Solid-State Lett.* **14**, C5 (2011).
- P. D. Ducharme, R. M. Asmussen, U. M. Tefashe, M. Danaie, W. J. Binns, P. Jakupi, G. A. Botton, D. W. Shoesmith, and J. Mauzeroll, *J. Electrochem. Soc.* **161**, C557 (2014).
- R. M. Asmussen, W. J. Binns, P. Jakupi, and D. Shoesmith, *J. Electrochem. Soc.* **161**, C501 (2014).
- N. D. Nam, W. C. Kim, J. G. Kim, K. S. Shin, and H. C. Jung, *J. Alloys Compd.* **509**, 4839 (2011).
- W. C. Kim, N. D. Nam, J. G. Kim, and J. I. Lee, *Electrochem. Solid-State Lett.* **14**, C21 (2011).
- N. D. Nam, M. Mathesh, M. Forsyth, and D. S. Jo, *J. Alloys Compd.* **542**, 199 (2012).
- D. Zander and N. A. Zumdieck, *Corros. Sci.* **93**, 222 (2015).
- K. H. Kim, N. D. Nam, J. G. Kim, K. S. Shin, and H. C. Jung, *Intermetallics* **19**, 1831 (2011).
- C. D. Yin, J. Yang, S. K. Woo, H. Y. Ha, and B. S. You, *Corros. Sci.* **90**, 597 (2015).
- J. Chen, Y. Song, D. Shan, and E. H. Han, *Corros. Sci.* **93**, 90 (2015).
- N. D. Nam, M. Mathesh, T. V. Le, and H. T. Nguyen, *J. Alloys Compd.* **616**, 662 (2014).
- Y. J. Chen, Z. Xu, C. Smith, and J. Sankar, *Acta Biomater.* **10**, 4561 (2014).
- E. Willbold, X. Gu, D. Albert, K. Kalla, K. Bobe, M. Brauneis, C. Janning, J. Nellesen, W. Czajka, W. Tillmann, Y. Zheng, and F. Witte, *Acta Biomater.* **11**, 554 (2015).
- Q. Chen and G. A. Thouas, *Mater. Sci. Eng. R: Reports* **87**, 1 (2015).
- D. T. Chou, D. Hong, P. Saha, J. Ferrero, B. Lee, Z. Tan, Z. Dong, and P. N. Kumta, *Acta Biomater.* **9**, 8518 (2013).
- M. Bornapour, N. Muja, D. Shum-Tim, M. Cerruti, and M. Pekguleryuz, *Acta Biomater.* **9**, 5319 (2013).
- Z. Li, X. Gu, S. Lou, and Y. Zheng, *Biomaterials* **29**, 1329 (2008).
- B. Denkena and A. Lucas, *Ann. CIRP* **56**, 113 (2007).
- M. B. Kannan and R. K. S. Raman, *Biomaterials* **29**, 2306 (2008).
- N. T. Kirkland, N. Birbilis, J. Walker, T. Woodfield, G. J. Dias, and M. P. Staiger, *J. Biomed. Mater. Res. B* **95**, 91 (2010).
- H. R. B. Rad, M. H. Idris, M. R. A. Kadir, and S. Farahany, *Mater. Des.* **33**, 88 (2012).
- Z. Li, X. Gu, S. Lou, and Y. Zheng, *Biomaterials* **29**, 1329 (2008).
- L. Hench and J. Polak, *Science* **295**, 1014 (2002).
- K. M. Hampshire and N. F. Krebs, *J. Nutr.* **137**, 1101 (2007).
- N. N. Greenwood and A. Eamshaw, *Chemistry of the Elements* 1997 (2nd ed.). Oxford: Butterworth-Heinemann.
- B. Zberg, P. J. Uggowitzer, and J. F. Loffler, *Nature Materials* **8**, 887 (2009).
- X. Gu, Y. Zheng, S. Zhong, T. Xi, J. Wang, and W. Wang, *Biomaterials* **31**, 1093 (2010).
- P. R. Cha, H. S. Han, G. F. Yang, Y. C. Kim, K. H. Hong, S. C. Lee, J. Y. Jung, J. P. Ahn, Y. Y. Kim, S. Y. Cho, J. Y. Byun, K. S. Lee, S. J. Yang, and H. K. Seok, *Sci. Rep.* **3**, 2367 (2013).
- E. Ma and J. Xu, *Nature Materials* **8**, 855 (2009).
- J. I. Post, J. K. Eibl, and G. M. Ross, *Amyotrophic Lateral Sclerosis* **9**, 149 (2008).
- H. R. B. Rad, M. H. Idris, M. R. A. Kadir, S. Farahany, A. Fereidouni, and M. Y. Yahya, *Applied Mechanics and Materials* **121**, 568 (2012).
- E. Zhang and L. Yang, *Materials Science and Engineering A* **497**, 111 (2008).
- M. Zamini, *Corrosion* **37**, 627 (1981).
- G. L. Makar and J. Kruger, *Int. Mater. Rev.* **38**, 138 (1993).
- H. R. B. Rad, E. Hamzah, A. F. Lotfabadi, M. Daroonparvar, M. A. M. Yajid, M. M. Islam, M. K. Asgarani, and M. Medraj, *Mater. Corros.* **65**, 1178 (2014).
- D. A. Jones, *Principles and Prevention of Corrosion* 1996, Prentice-Hall, Upper Saddle River, NJ.
- K. H. Kim, S. H. Lee, N. D. Nam, and J. G. Kim, *Corros. Sci.* **53**, 3576 (2011).
- Q. V. Bui, N. D. Nam, B. I. Noh, A. Kar, J. G. Kim, and S.-B. Jung, *Mater. Corros.* **61**, 30 (2010).
- J. R. MacDonald, *Impedance Spectroscopy* 1987, Wiley, New York.
- D. C. Silverman, *Corrosion prediction from circuit models application to evaluation of corrosion inhibitors, electrochemical impedance. Analysis and interpretation* 1993, ASTM STP 1188, in: J. R. Scully, D. C. Silverman, and M. W. Kendig, American Society for Testing and Materials, Philadelphia.
- ASM International, *Metals Handbook* 1987, ninth ed., Corrosion, ASM International, Vol. 13.
- J. C. Riviere and S. Myhra, *Handbook of Surface and Interface Analysis: Methods for Problem-Solving* 1998, Marcel Dekker, Inc. New York.
- A. Talapatra, S. K. Bandyopadhyay, P. Sen, P. Barat, S. Mukherjee, and M. Mukherjee, *Physica C* **419**, 141 (2005).
- S. P. Kowalezyk, L. Ley, F. R. McFeely, R. A. Pollak, and D. A. Shirley, *Phys. Rev. B* **9**, 381 (1974).
- B. Demri and D. Muster, *J. Mater. Process. Technol.* **55**, 311 (1995).
- C. J. Powell, *J. Electron Spectrosc. Relat. Phenom.* **185**, 1 (2012).
- Evan Ma and Jian Xu, *Nature Mater.* **8**, 855 (2009).
- A. L. Greer and E. Ma, *MRS Bull.* **32**, 611 (2007).